Neutron scattering study of magnetic excitations in a 5d-based double-perovskite Ba₂FeReO₆

K. W. Plumb,[1] A. M. Cook,[1] J. P. Clancy,[1] A. I. Kolesnikov,[2] B. C. Jeon,[3] T. W. Noh,[3] A. Paramekanti,[1,4] and Young-June Kim[1]

[1]*Department of Physics, University of Toronto, Toronto, Ontario M5S 1A7, Canada*

[2]*Neutron Scattering Sciences Division, Oak Ridge National Laboratory, Oak Ridge, Tennessee 37831, USA*

[3]*Center for Functional Interfaces of Correlated Electron Systems, Institute for Basic Science, and Department of Physics and Astronomy,*
Seoul National University, Seoul 151-747, Korea

[4]*Canadian Institute for Advanced Research, Toronto, Ontario M5G 1Z8, Canada*

Motivated by exploring spin-orbit-coupled magnetism in 5d-based transition metal oxides (TMOs) beyond the iridates, we present a powder inelastic neutron scattering study of magnetic excitations in Ba₂FeReO₆—a member of the double-perovskite family of materials which exhibit half-metallic behavior and high Curie temperatures T_c. We find clear evidence of two well-defined dispersing magnetic modes in its low-temperature ferrimagnetic state. We develop a local moment model, which incorporates the interaction of Fe spins with spin-orbital locked magnetic moments on Re and show that it captures our experimental observations. This allows us to extract moment sizes and exchange couplings, explain the magnitude of T_c, and infer that magnetostructural locking terms are weak. Our study further opens up Re-based compounds as model systems to explore the interplay of strong correlations and spin-orbit coupling in 5d TMOs.

I. INTRODUCTION

Strong electronic correlations in the 3d and 4d transition-metal oxides (TMOs) lead to such remarkable phenomena as high-temperature superconductivity in the cuprates,[1] colossal magnetoresistance in the manganites,[2] and possible chiral superconductivity in the ruthenates.[3] In 5d TMOs, the traditional viewpoint suggests that the larger spread of atomic wave functions leads to a smaller local Hubbard repulsion and a larger overlap between neighboring atomic orbitals, which cooperate to suppress strong correlation effects. Indeed, simple oxides like ReO₃ are good metals.[4] This traditional picture has been challenged by recent work on iridium-based complex oxides, which shows that the large spin-orbit (SO) coupling on Ir can split the t_{2g} crystal field levels, yielding a reduced bandwidth for effective $j_{\rm eff} = 1/2$ electrons and the re-emergence of strong correlations.[5] Iridates like Na₂IrO₃, Na₄Ir₃O₈, Eu₂Ir₂O₇, and Y₂Ir₂O₇ are of great interest since they may support correlated SO-coupled magnetism or topological phases.[6–14]

Despite these remarkable developments in the iridates, there are good reasons to also explore spin-orbit coupling physics in other 5d TMOs. (i) In contrast to the iridates, where Ir is a strong neutron absorber, other TMOs such as those based on Re can permit a careful study of the spin-orbital dynamics via inelastic neutron scattering experiments. Such studies are valuable for an eventual complete understanding of the magnetism. (ii) While the iridates have been described by an effective one-band $j_{\rm eff} = 1/2$ model with Hubbard correlations, other 5d elements may exhibit distinct phenomena associated with the regime where multiorbital interactions and Hund's coupling conspire with spin-orbit coupling to give rise to new physics. For example, there are two electrons in 5d orbitals (d^2) in Re²⁺. Even in the presence of strong spin-orbit coupling and cubic crystal field, the electronic state is not described by simply filling $j_{\rm eff} = 3/2$ single-particle states with two electrons. We find that nonzero Hund's coupling should be considered in addition to spin-orbit coupling,[15] and angular momentum in this case is described by a $j_{\rm eff} = 2$ state.

(iii) Some aspects of the iridates still appear to be controversial, for example, whether the insulating states and magnetism in Na₂IrO₃ and Sr₂IrO₄ arise from $j_{\rm eff} = 1/2$ Mott physics[5–7,16] or from undergoing a Slater transition.[17–19] Exploring simpler 5d TMOs where one has a careful experimental and theoretical understanding of the SO-coupled magnetism may provide a useful perspective on such issues.

Motivated by these considerations, we focus here on a 5d Re-based double-perovskite material, Ba₂FeReO₆ (see Fig. 1). This general class of double-perovskite (DP) compounds A₂BB′O₆ is also of great interest since materials like A₂FeReO₆ (A = Ca,Sr,Ba),[20–29] Sr₂FeMoO₆,[30] and Sr₂CrOsO₆,[31,32] with a 3d magnetic B ion and a 5d B′ ion, exhibit high ferromagnetic Curie temperatures. In addition, the half-metallic character and significant polarization of many DPs makes them ideal candidates for spintronic applications such as spin injection.[33,34]

In this paper, we use inelastic neutron scattering (INS) on polycrystalline Ba₂FeReO₆ to study the magnetic excitations in its ferrimagnetic state, complemented by a theoretical modeling of the observed spectrum. Our main results, which are summarized in Fig. 2, are as follows. (i) We provide experimental evidence of *two* dispersive magnetic modes in the magnetic excitation spectrum, showing that Fe and Re electrons both exhibit strong correlations and contribute to the magnetization dynamics. (ii) Remarkably, we find evidence of nearly gapless magnetic excitations in the inelastic spectrum, indicating that despite the strong SOC, there is only a weak locking of Re moments to the lattice in the ferrimagnetic state. (iii) We discuss a minimal local moment model of strongly coupled spin and orbital degrees of freedom on Re interacting with spins on Fe and show that this captures our experimental observations extremely well. (iv) We combine our results with published magnetization[35] and x-ray magnetic circular dichroism (XMCD) data[24] to obtain quantitative estimates of the Re and Fe moments and the effective Re-Fe exchange interaction. (v) We find evidence in the neutron scattering data which is suggestive of spin-phonon interactions, likely
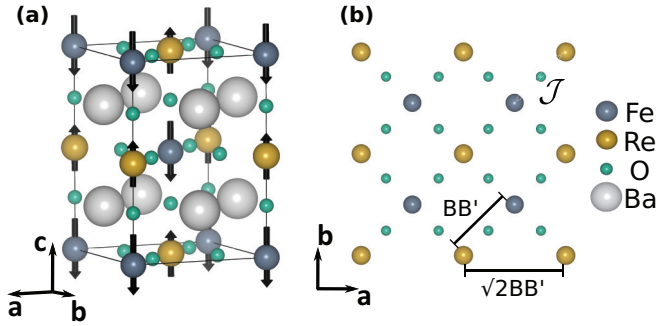
FIG. 1. (Color online) Crystal structure of Ba_2FeReO_6. (a) Schematic of the crystallographic unit cell showing the relative orientation of Fe and Re moments. (b) Projection into the ab plane illustrating the separation between B(B′) site ions and the exchange pathway $\mathcal{J}$ between neighboring Fe and Re sites.

mediated by the strong spin-orbit coupling. Such spin-phonon coupling has also been inferred in a recent Raman scattering study.[26] Our combined experimental and theoretical work thus further opens up Re-based TMOs as model systems to study the interplay of spin-orbit coupling and strong electronic correlations. The inelastic neutron scattering results will be presented first in Sec. II, and details of the theory are contained in Sec. III and Appendix A.

II. EXPERIMENTS

A total of 8.6 g of polycrystalline Ba_2FeReO_6 was synthesized using the standard solid-state method reported
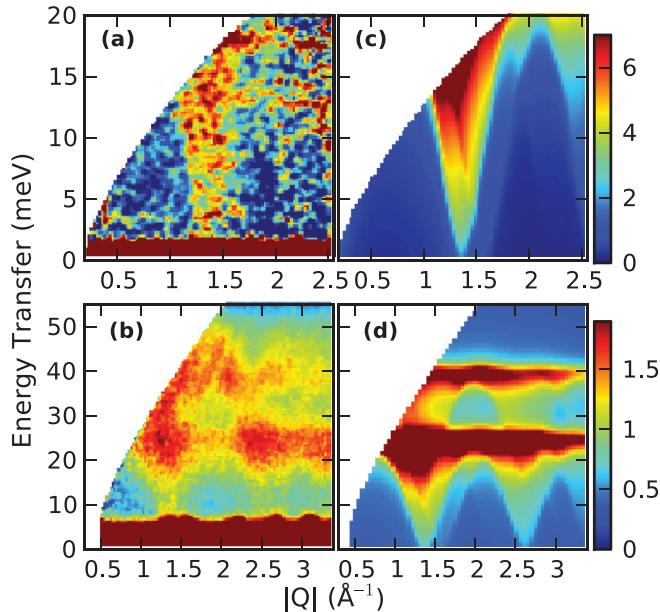

FIG. 2. (Color online) Comparison of spin wave model and measured powder-averaged magnetic scattering intensity for $T = 34$ K. An empty Al-Can background signal has been subtracted from the data. [(a) and (b)] Neutron scattering data for incident energies of 27 and 120 meV, respectively. [(c) and (d)] Powder-averaged dynamic structure factor calculated from the spin wave model with $6\mathcal{J}_{eff}\mathcal{F} = 39$ meV and $6\mathcal{J}_{eff}\mathcal{R} = 25$ meV.

previously.[25,35] In some DPs, antisite disorder (mixing of B and B′ site atoms) is significant and suppresses saturated magnetic moments. However, for Ba_2FeReO_6, a large difference (~8%) in the ionic radii of Fe^{3+} and Re^{5+} seems to mitigate this problem. From the structural refinement of x-ray powder diffraction data, we infer an antisite disorder of $\lesssim 1\%$, consistent with that reported by Winkler *et al.*[36]

Neutron scattering measurements were carried out on the fine-resolution Fermi-chopper spectrometer SEQUOIA[37,38] at the Spallation Neutron Source (SNS) at Oak Ridge National Laboratory (ORNL). Measurements were performed with Fermi chopper 1 rotating at a frequency of 300 Hz and phased for incident energies of 27 and 120 meV. A T0 chopper rotating at 180 Hz was used to eliminate a fast neutron background. The sample was sealed in an Al can and mounted on a closed cycle cryostat. Data were also collected for an empty Al sample can at $T = 34$ K, with an identical instrumental configuration. The absorption corrected empty can intensities were subtracted from the raw data at $T = 34$ K to remove scattering from the sample environment.

Throughout this article we use pseudocubic notation $a = b = c \approx 4.01$ Å and index the momentum transfer **Q** in units of $1/a$ to aid comparison with theoretical calculations. In our magnetic model ferrimagnetism arises from G-type antiferromagnetic arrangement of inequivalent Fe and Re moments so magnetic Bragg peaks occur at the antiferromagnetic wave vector $\mathbf{Q}_{AF} = (\pi,\pi,\pi)$ and the ferromagnetic wave vector $\mathbf{Q}_{FM} = (2\pi,0,0)$.

Maps of the inelastic neutron scattering intensity for 27- and 120-meV incident neutron energies are shown in Figs. 2(a) and 2(b), respectively. An inelastic feature emanating from $Q = 1.35$ Å⁻¹ corresponding to $\mathbf{Q}_{AF}$ is clearly resolved. The inelastic feature extends into two bands of excitations with maximum intensities near 25 and 39 meV. The scattering is strongest at low Q and decays rapidly for increasing Q, as is expected generally from the form factor dependence for magnetic scattering. Results from our theoretical model are shown in Figs. 2(c) and 2(d) with the best-fit parameters.

The temperature and energy dependence of putative magnetic scattering in Ba_2FeReO_6 is presented in Fig. 3. Bragg peaks at $Q = 1.35$ Å⁻¹ corresponding to $\mathbf{Q}_{AF}$ and $Q = 1.56$ Å⁻¹ corresponding to $\mathbf{Q}_{FM}$ are shown in Fig. 3(a). The elastic magnetic intensity decreases on warming and the antiferromagnetic Bragg peak vanishes above 300 K, consistent with $T_c \approx 304$ K reported from uniform magnetization[35] and powder neutron diffraction measurements.[24] Magnetic elastic scattering at $\mathbf{Q}_{FM}$ is superposed on a structural Bragg reflection so it is more difficult to discern the temperature-dependent intensity resulting from magnetic scattering at this **Q** position.

Constant momentum transfer cuts detailing the inelastic scattering emerging from the magnetic zone center are shown in Fig. 3(b). The fluctuation-dissipation theorem $S(Q,E) = [n(E,T) + 1]\chi''(Q,E)$ relates the imaginary component of the dynamic susceptibility $\chi''(Q,E)$ to the dynamic structure factor measured by neutron scattering where $n(E,T)$ is the Bose thermal occupation factor. Correcting the INS intensity by the Bose factor allows for comparison of the inelastic scattering across the entire 400 K temperature range on a single intensity scale. Two strong inelastic features are visible near 25 and 39 meV which decrease in intensity on increasing
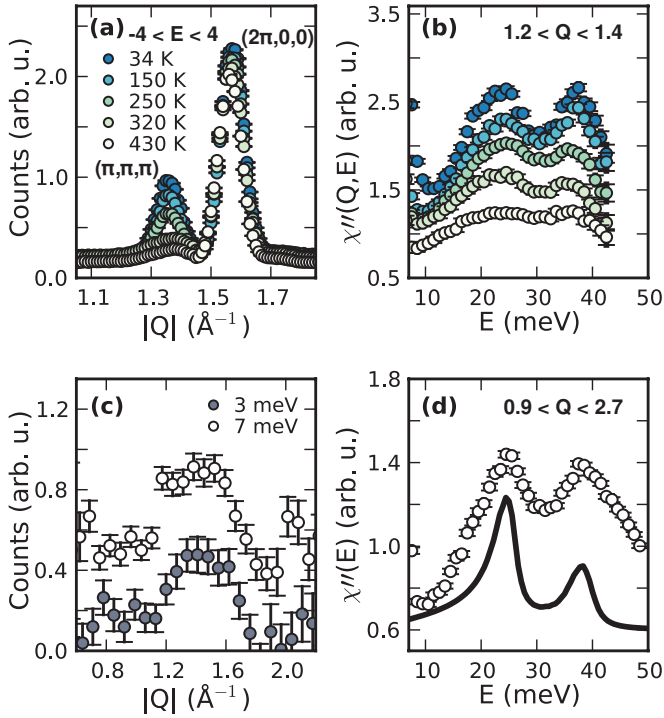
FIG. 3. (Color online) Representative cuts through $S(Q,E)$. (a) Temperature dependence of magnetic Bragg peaks at $\{\pi,\pi,\pi\}$ and $\{2\pi,0,0\}$ determined by integrating the $E_i = 120$ meV data over the elastic line resolution $[-4 < E < 4$ meV]. (b) Temperature dependence of Bose factor corrected inelastic scattering near the magnetic zone center. (c) Constant energy cuts from the $E_i = 27$ meV data at 34 K; each energy cut was integrated over ± 1 meV, and the 7-meV cut is offset for clarity. (d) Bose factor–corrected inelastic scattering at 34 K integrated over a magnetic Brillouin zone representing the magnetic density of states; the solid line is an equivalent cut from the spin-wave-model calculation. An empty-can background has been subtracted from the data in (c) and (d).

temperature. The temperature, momentum, and energy dependence of the low-Q inelastic scattering is entirely consistent with expectations for scattering from powder-averaged spin waves. Broader examination of the data reveals two bands of phonon scattering which partially obscures the magnetic signal above 3 Å^{-1}; however, the phonon and magnetic scattering are well resolved since the magnetic form factor rapidly attenuates the magnetic intensity with increasing Q while the phonon scattering intensity increases with Q (see Appendix B).

Constant energy cuts across the low-energy magnetic scattering are shown in Fig. 3(c). An inelastic feature emerging from the antiferromagnetic zone center is clearly resolved within our experimental resolution down to at least 3 meV. The scattering intensity is strongest near the antiferromagnetic wave vector at $Q = 1.35$ Å^{-1} (where the structure factor for magnetic scattering is maximized) and is small near the nuclear Bragg peak. This Q dependence identifies the low-energy inelastic scattering as magnetic in origin and places an upper bound of 3 meV for any gap in the spin wave dispersion. The Q-integrated inelastic intensity is peaked at the magnon zone boundary energy where the density of states for spin waves is maximized, enabling a precise determination of the zone-boundary energies from the powder-averaged spectrum. The

dynamic susceptibility integrated over the magnetic Brillouin zone is shown in Fig. 3(d); scattering is strongly peaked at 25 and 39 meV. An equivalent cut from the powder-averaged spin wave theory using the same parameters as in Figs. 2(c) and 2(d) is also shown in the figure.[39]

III. Theory and comparison with experiment

The two well-defined magnetic modes in Fig. 2, and the fact that the closely related material Ca_2FeReO_6 is an insulator, suggest that strong electronic correlations are important in Ba_2FeReO_6 on both Re and Fe. A local moment model thus provides a useful vantage point to describe its magnetic excitations.

A. Local moment model

On the Fe sites, a nominal valence assignment of Fe^{3+} together with a strong Hund's coupling leads to orbital moment quenching and a spin $\mathcal{F} = 5/2$. On the Re sites, a nominal valence assignment of Re^{5+} ($5d^2$) leads to two electrons in the t_{2g} orbital. Thus, in contrast to the iridates, not only SOC but also Hund's coupling (J_H) is important in determining the magnetic state on Re.[15] The atomic Hamiltonian, when projected to the t_{2g} orbital,[40] takes the form

$$H_{Re} = -2J_H \vec{S}^2 - \frac{J_H}{2}\vec{L}^2 - \lambda(\vec{\ell}_1 \cdot \vec{s}_1 + \vec{\ell}_2 \cdot \vec{s}_2), \quad (1)$$

where $\vec{S} = \vec{s}_1 + \vec{s}_2$ and $\vec{L} = \vec{\ell}_1 + \vec{\ell}_2$. The Hund's coupling is expected to drive the two electrons into a spin symmetric state with $S = 1$ and an orbitally antisymmetric state with $L = 1$. Indeed, as shown in Fig. 4(a), H_{Re} supports a fivefold
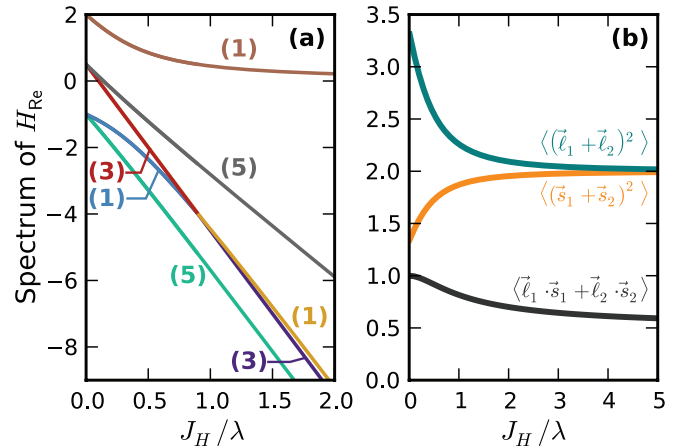

FIG. 4. (Color online) (a) Spectrum of H_{Re} (in units of λ) versus J_H/λ, with degeneracies indicated in brackets. For $J_H = 0$, the eigenstates at three distinct energies correspond to different ways of filling two electrons into SO-coupled single-particle states with angular momentum $j = 3/2$ and $j = 1/2$. When $\lambda = 0$, we find two-particle angular-momentum eigenstates ^3P, ^1D, and ^1S in increasing order of energy. A weak SO coupling, with $J_H/\lambda \gg 1$, splits the lowest ^3P manifold into $^3P_2$, $^3P_1$, and $^3P_0$. (b) Interaction dependence of total orbital and spin angular momentum and magnitude of SO energy. For $J_H \gtrsim 2\lambda$, the ground state is composed of $L = 1, S = 1$ moments, which lock to yield a total angular momentum $\vec{\mathcal{R}} = \vec{L} + \vec{S}$, with $\mathcal{R} = 2$.

degenerate ground state over a wide range of J_H/λ (see Appendix A for details). For $J_H/\lambda \gtrsim 2$, which appears to be quite reasonable, we find as seen in Fig. 4(b) that this ground-state manifold may be viewed as made of $L = 1$ and $S = 1$ moments locked into a state with total angular momentum $\vec{\mathcal{R}} = \vec{L} + \vec{S}$, with $\mathcal{R} = 2$.[41]

The simplest local moment Hamiltonian for Ba_2FeReO_6 is, thus,

$$H = \mathcal{J} \sum_{\langle \mathbf{rr'} \rangle} \vec{S}_{\mathbf{r}} \cdot \vec{\mathcal{F}}_{\mathbf{r'}} - \lambda \sum_{\mathbf{r} \in Re} \vec{L}_{\mathbf{r}} \cdot \vec{S}_{\mathbf{r}}, \qquad (2)$$

with a nearest-neighbor antiferromagnetic exchange interaction between the Fe spin $\vec{\mathcal{F}}$ and the Re spin $\vec{S}$ induced by intersite tunneling, and λ denotes the spin-orbit coupling. This simple model should be more broadly applicable to many DPs $A_2BB'O_6$ with an orbitally nondegenerate magnetic B site and a magnetic B' site with two electrons in an active t_{2g} orbital.

For Ba_2FeReO_6, where spin-orbit coupling is expected to be strong, $\lambda \gg \mathcal{J}$, and the local moment Hamiltonian simplifies to

$$H_{\text{eff}} = \mathcal{J}_{\text{eff}} \sum_{\langle \mathbf{rr'} \rangle} \vec{\mathcal{R}}_{\mathbf{r}} \cdot \vec{\mathcal{F}}_{\mathbf{r'}}, \qquad (3)$$

yielding an effective Heisenberg model with moments $\mathcal{R}, \mathcal{F}$ on the Re and Fe sites, respectively. We find that

$$\mathcal{J}_{\text{eff}} = \mathcal{J} \frac{\mathcal{R}(\mathcal{R}+1) + S(S+1) - L(L+1)}{2\mathcal{R}(\mathcal{R}+1)}. \qquad (4)$$

For $L = S = 1$ and $\mathcal{R} = 2$, we obtain $\mathcal{J}_{\text{eff}} = \mathcal{J}/2$.

We expect that the metallic nature of Ba_2FeReO_6, and the concomitant carrier delocalization, will lead to a smaller effective value of $\mathcal{F}, \mathcal{R}$ compared to this highly localized viewpoint. This is borne out in our detailed comparisons with experiments discussed below.

B. Spin wave dispersion

The model H_{eff} has a ferrimagnetic ground state, with antiferromagnetic order of $\vec{\mathcal{F}}$ and $\vec{\mathcal{R}}$ leading to a net ordered moment. A spin-wave calculation[42] around this ground state yields two modes, with energies $\Omega_{\pm}(\mathbf{Q}) = \sqrt{\mathcal{S}_+^2 \gamma_0^2 - \mathcal{F}\mathcal{R}\gamma_{\mathbf{Q}}^2} \pm \mathcal{S}_- \gamma_0$, where $\mathcal{S}_{\pm} = (\mathcal{F} \pm \mathcal{R})/2$, and $\gamma_{\mathbf{Q}} = 2\mathcal{J}_{\text{eff}}(\cos Q_x + \cos Q_y + \cos Q_z)$, with $\gamma_0 = 6\mathcal{J}_{\text{eff}}$. At $\mathbf{Q} = (0,0,0)$ and (π,π,π), Ω_- has a gapless quadratic dispersion, while Ω_+ has a gap $2\mathcal{S}_- \gamma_0$. At $T = 0$, we find the dynamic structure factor for transverse spin fluctuations

$$S_{\perp}(\mathbf{Q}, \omega) = 2\pi \sum_{\sigma = \pm} (G_{\mathbf{Q}} - \sigma \mathcal{S}_-) \delta[\omega - \Omega_{\sigma}(\mathbf{Q})], \qquad (5)$$

where $G_{\mathbf{Q}} = (\gamma_0 \mathcal{S}_+^2 - \gamma_{\mathbf{Q}} \mathcal{F}\mathcal{R})/\sqrt{\mathcal{S}_+^2 \gamma_0^2 - \mathcal{F}\mathcal{R}\gamma_{\mathbf{Q}}^2}$. As shown in Figs. 2(a)–2(d) and Fig. 3(d), setting $\gamma_0 \mathcal{F} = 39$ meV and $\gamma_0 \mathcal{R} = 25$ meV in the theoretical plots leads to a broad agreement between the experimental data and the powder-averaged theoretical result for $S(\mathbf{Q}, \omega)$, both in the existence and dispersion of the two magnetic modes, and in the (near) gaplessness of the lower energy mode. The ratio of the magnetic intensities at $\mathbf{Q} = (\pi,\pi,\pi)$ to $\mathbf{Q} = (2\pi,0,0)$ is given by $(\mathcal{S}_+/\mathcal{S}_-)^2$, which can be very large. As a result,

the "antiferromagnetic" fluctuations near $\mathbf{Q} = (\pi,\pi,\pi)$ are much more visible than the "ferromagnetic" fluctuations near $\mathbf{Q} = (2\pi,0,0)$.

C. Spin-orbital locking on Re, moment sizes, exchange couplings

For momenta with $\gamma_{\mathbf{Q}} = 0$, the spin-wave dispersion yields $\Omega_+/\Omega_- = \mathcal{F}/\mathcal{R}$. Since these momenta dominate the magnon density of states, we can use the ratio of the observed peak positions in Fig. 3 (39 meV, 25 meV) to deduce that $\mathcal{F}/\mathcal{R} \approx 1.6$. If we assume that the Re moments have a pure spin origin, we have to set $\mathcal{R} \lesssim 1$. This assumption, however, yields a Fe spin $\mathcal{F} \lesssim 1.6$, which is anomalously low: First-principles calculations,[25,43] a naïve valence assignment of Fe^{3+}, and the measured large saturation magnetization[35] all point to a much larger Fe moment. Our observations thus strongly suggest that we must have $\mathcal{R} > 1$, indicating a nonzero orbital contribution to the Re moment, in qualitative agreement with XMCD measurements.[24]

In order to obtain estimates of the moment sizes and the exchange coupling, we combine our INS results with previous XMCD[24] and magnetization[35] data. XMCD measurements[24] indicate a significant static orbital contribution to the magnetization on Re, with $\mu_{\text{Re}}^{\text{orb}}/\mu_{\text{Re}}^{\text{spin}} \approx -0.3$. This allows us to set $L \approx 0.6S$, which yields $S \approx 0.63\mathcal{R}$ and $L \approx 0.37\mathcal{R}$. High field magnetization measurements on Ba_2FeReO_6 indicate a saturation magnetization $m_{\text{sat}} \approx 3\mu_B$. Together with our neutron data, this constrains the moment sizes to be $\mathcal{R} \approx 1.3$ and $\mathcal{F} \approx 2.1$, yielding an estimated exchange coupling $\mathcal{J}_{\text{eff}} \approx 3.1$ meV, so $\mathcal{J} \approx 6$ meV.

We have checked that including a small direct Re-Re Heisenberg exchange $\sim 0.1\mathcal{J}_{\text{eff}}$ slightly modifies the spin-wave dispersion and our exchange constant estimates, but does not significantly affect, our estimate of $\mathcal{R}$. A large Re-Re exchange coupling $\gtrsim 0.2$–$0.3\mathcal{J}_{\text{eff}}$ leads to a dispersion which is not consistent with our data. The estimated magnitude of the exchange coupling and the absence of a strong frustrating Re-Re interaction may have important implications for the theoretical modeling[30] of the closely related insulating DP, Sr_2CrOsO_6. Thus, while previous XMCD measurements[24] on Ba_2FeReO_6 have shown that there is a static orbital contribution to the ordered magnetic moment on Re in the ferrimagnetic state, our work shows that such SO locked moments on Re also play a role in the low-energy magnetic *excitations*.

D. Structural transition and absence of spin gap

Ba_2FeReO_6 has a weak tetragonal distortion, with $c/a < 1$, which onsets at the magnetic T_c.[24] Since a Jahn-Teller distortion would lead to $c/a > 1$, not necessarily coincident with T_c, we ascribe this distortion to SOC. Going beyond H_{eff}, we expect a term $-\epsilon \sum_{\mathbf{r}} (\mathcal{R}_{\mathbf{r},x}^4 + \mathcal{R}_{\mathbf{r},y}^4 + \mathcal{R}_{\mathbf{r},z}^4)$, arising from the cubic anisotropy, which locks the Re moment (and thus also the Fe spins) to the crystal axes. Such a magnetostructural locking term with $\epsilon > 0$ explains the observed tetragonal distortion at T_c as arising from weak orbital order and would lead to a spin gap of order ϵ. This locking is expected to be small since it arises from a spin-orbit induced weak mixing

of well-separated t_{2g} and e_g crystal field levels.[15] This is consistent with our experimental observations—we find no clear evidence of a spin gap down to ~ 1 meV. A very small magnetostructural locking term is also consistent with the measured weak coercive field ~ 0.2 T.

E. Magnetic transition temperature

We use the above values of the moment sizes and exchange couplings to estimate the magnetic T_c. The nearest-neighbor classical Heisenberg model on a three-dimensional cubic lattice, with moments $\mathcal{F},\mathcal{R}$ on the two sublattices, has a mean-field transition temperature $2\mathcal{J}_{\text{eff}}\mathcal{F}\mathcal{R}$. Assuming a quantum renormalized $T_c \approx 2\mathcal{J}_{\text{eff}}\sqrt{\mathcal{F}\mathcal{R}}(\sqrt{\mathcal{F}\mathcal{R}}+1)$, we estimate $T_c \approx 315$ K, in rough agreement with the measured $T_c^{\text{expt}} \approx 304$ K. If one takes the limit of fully localized moments, setting $\mathcal{F} = 2.5$ and $\mathcal{R} = 2$, one obtains $T_c \approx 520$ K, remarkably close to that of the insulating compound Ca_2FeReO_6. T_c calculations retaining the itinerant Re electrons will be reported elsewhere.

IV. SUMMARY

We have used inelastic neutron scattering and theoretical modeling to study the magnetic excitations in Ba_2FeReO_6, inferring the presence of strong correlations and spin-orbit-coupled moments on Re and obtaining a broad understanding of the phenomenology in its ferrimagnetic state. Further efforts are necessary to synthesize single crystals or good-quality thin films of Ba_2FeReO_6 and other DPs. In future work, we will extend our experiments to other DP materials and incorporate the itinerant character of Re electrons in our theoretical modelling, both of which would lead to a better understanding of novel $5d$-based TMOs.

ACKNOWLEDGMENTS

APPENDIX A: INTERACTION EFFECTS—ATOMIC LIMIT

For the $d^{(2)}$, $d^{(3)}$, $d^{(4)}$ configuration of electrons in the t_{2g} orbital, we have to consider matrix elements of the Coulomb interaction on the same footing as the spin-orbit coupling. The interaction Hamiltonian projected to the t_{2g} orbitals is given by[44]

$$H_{\text{int}} = U \sum_\alpha n_{\alpha\uparrow} n_{\alpha\downarrow} + \left(U - 5\frac{J_H}{2}\right)\sum_{\alpha<\beta} n_\alpha n_\beta$$
$$- 2J_H \sum_{\alpha<\beta} \vec{S}_\alpha \cdot \vec{S}_\beta + J_H \sum_{\alpha\neq\beta} d^\dagger_{\alpha\uparrow} d^\dagger_{\alpha\downarrow} d_{\beta\downarrow} d_{\beta,\uparrow}. \quad (A1)$$

After some algebra, this can be re-expressed in terms of rotationally invariant operators as

$$H_{\text{int}} = \frac{U - 3J_H}{2} n_{\text{tot}}^2 - 2J_H \vec{S}_{\text{tot}}^2 - \frac{J_H}{2}\vec{L}_{\text{tot}}^2, \quad (A2)$$

where we assume the normal ordered form of these operators. For a $d^{(2)}$ configuration, $n_{\text{tot}} = 2$. Including the spin-orbit-coupling term leads to the effective atomic Hamiltonian for Re,

$$H_{\text{Re}} = -2J_H \vec{S}^2 - \frac{J_H}{2}\vec{L}^2 - \lambda(\vec{\ell}_1 \cdot \vec{s}_1 + \vec{\ell}_2 \cdot \vec{s}_2), \quad (A3)$$

where $\vec{L} = \vec{\ell}_1 + \vec{\ell}_2$ and $\vec{S} = \vec{s}_1 + \vec{s}_2$. To diagonalize this Hamiltonian for a $d^{(2)}$ configuration, we write the full Hamiltonian in the basis $|L,m_\ell,S,m_s\rangle$ corresponding to total orbital and total spin angular momentum. Since the individual orbital angular momenta $\ell_1 = \ell_2 = 1$ and individual spin angular momenta are $s_1 = s_2 = 1/2$, we use a shorthand for the Clebsch-Gordan coefficients, defining them via

$$|L,m_\ell,S,m_s\rangle = |L,m_\ell\rangle \otimes |S,m_s\rangle, \quad (A4)$$

$$|L,m_\ell\rangle = \sum_{m_1,m_2} C^{L,m_\ell}_{m_1,m_2}|m1,m2\rangle, \quad (A5)$$

$$|S,m_s\rangle = \sum_{s_1,s_2} C^{S,m_s}_{s_1,s_2}|s1,s2\rangle, \quad (A6)$$

in terms of which the full Hamiltonian becomes

$$\langle L',m'_\ell,S',m'_s|H^{(2)}_{\text{at}}|L,m_\ell,S,m_s\rangle \equiv H^{L',m'_\ell,S',m'_s}_{L,m_\ell,S,m_s}, \quad (A7)$$

where

$$H^{L',m'_\ell,S',m'_s}_{L,m_\ell,S,m_s} = \delta_{L,L'}\delta_{S,S'}\delta_{m'_\ell,m_\ell}\delta_{m'_s,m_s} E_{L,S}$$
$$- \lambda \sum_{m_1,m_2,s_1,s_2} C^{L,m_\ell}_{m_1,m_2} C^{S,m_s}_{s_1,s_2} \left(2m_1 s_1 \bar{C}^{L',m'_\ell}_{m_1,m_2}\bar{C}^{S',m'_s}_{s_1,s_2}\right.$$
$$\left. + \sqrt{2}\bar{C}^{L',m'_\ell}_{m_1+1,m_2}\bar{C}^{S',m'_s}_{s_1-1,s_2} + \sqrt{2}\bar{C}^{L',m'_\ell}_{m_1-1,m_2}\bar{C}^{S',m'_s}_{s_1+1,s_2}\right)$$
$$(A8)$$

and

$$E_{L,S} = \left[-2J_H S(S+1) - \frac{J_H}{2}L(L+1)\right]. \quad (A9)$$

Here, we must restrict ourselves to totally antisymmetric electronic states; $(L,S) = (0,0),(1,1),(2,0)$ yield the allowed 15 basis states.

When $J_H = 0$, we find eigenstates at three distinct energies corresponding to filling two electrons into single-particle states corresponding to a low-energy $j = 3/2$ manifold or a higher-energy $j = 1/2$ doublet. On the other hand, when $\lambda = 0$, we find H_{Re} has, in increasing order of energy, total angular-momentum eigenstates ^3P, ^1D, and ^1S.

The numerically computed spectrum of H_{Re} is shown in Fig. 4 of the paper. Over a wide range of J_H/λ, we find a fivefold degenerate ground state when spin-orbit coupling competes with J_H. For $J_H/\lambda \gg 1$, we can show that the ^3P ground states at $\lambda = 0$ split into spin-orbit-coupled states which may be labeled by total angular momentum $L + S = 2,1,0$ in increasing order of energy (corresponding to $^3P_2, ^3P_1, ^3P_0$ states with degeneracies 5,3,1). This shows that a local $-\lambda\vec{L}\cdot\vec{S}$, with $L = S = 1$, is a good description of the
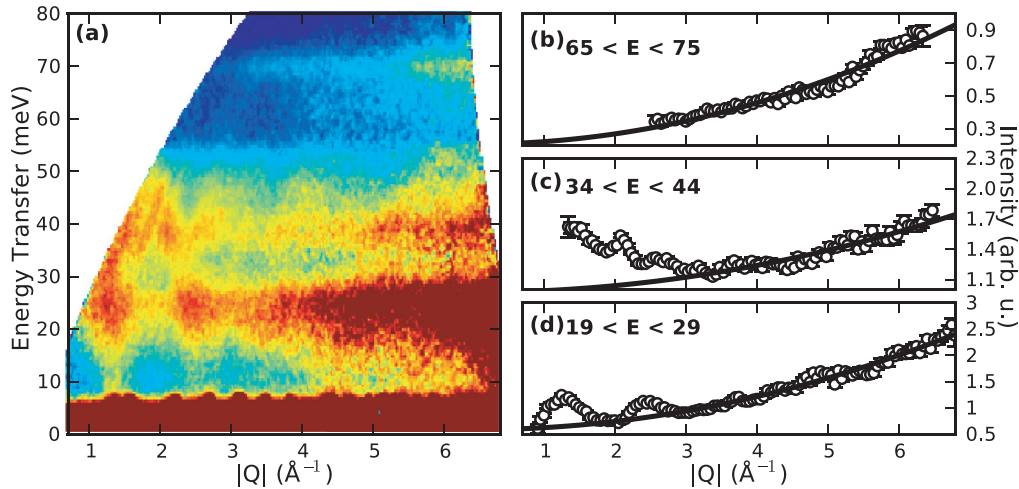
FIG. 5. (Color online) (a) Neutron scattering intensity at 34 K for and incident energy of 120 meV. An empty Al-can background has been subtracted from the data. [(b)–(d)] Constant energy cuts across bands of inelastic scattering at 70, 40, and 25 meV, respectively. Solid black lines are a fit to $I(Q) = A(E) + BQ^2$ delimiting the Q-dependent contribution of phonon scattering at each energy.

lowest-energy manifold of states when $J_H/\lambda \gtrsim 2$. However, when $J_H \lesssim \lambda$, this sequence changes to 5,1,3 (in ascending order) suggesting that such a simple description fails.

APPENDIX B: PHONON BACKGROUND

The measured scattering intensity consists of a number of components, including coherent nuclear and magnetic scattering, as well as incoherent processes. Additional background scattering originating from the sample environment and detector dark current are eliminated by subtracting the signal measured for an empty Al sample can using identical instrumental configuration. The signal of interest is coherent scattering from magnons, which has a momentum-dependent intensity dominated by the magnetic form factor. In general, the magnetic form factor rapidly decays as a function of Q, thus the magnetic INS intensity will decrease with increasing Q. In contrast, both coherent scattering from phonons and incoherent nuclear scattering intensities increase quadratically with Q in a powder-averaged measurement.[45] Any periodic modulations of the coherent phonon scattering arising from the structure factor should also increase in intensity with Q.

A map of the inelastic neutron scattering at 34 K, for 120-meV incident energy, is shown in Fig. 5(a). There are three bands of inelastic scattering, around 25, 40, and 70 meV, which increase in intensity with increasing Q. We associate each of these with three phonon bands. The magnetic signal emerges from the antiferromagnetic zone

center at $Q = 1.35$ Å^{-1} and extends into two bands with maximum intensities at 25 and 39 meV.

To highlight the momentum dependence of the scattering intensities, constant energy cuts through each band of inelastic scattering are shown in Figs. 5(b)–5(d). Around 70 meV [Fig. 5(b)], the scattering is dominated by phonons, and here the momentum dependence of scattering intensity is entirely described by the quadratic form $I(Q) = A(E) + BQ^2$, where A is a constant function of Q parameterizing background originating from the small multiple scattering contributions to the inelastic scattering. On average, A is a decaying function of energy. In Figs. 5(c) and 5(d) the overall intensity increases with increasing Q at high Q, and above $Q = 3$ Å^{-1} the scattering is dominated by phonons, as can be seen from the fits to $I(Q)$ (solid black lines). However, below $Q = 3$ Å^{-1} the INS intensity clearly increases above the phonon background with decreasing Q. Furthermore, in Fig. 5(d), the low Q scattering intensity modulation is consistent with the magnetic Brillouin zone. Thus, the magnetic scattering is well separated in Q from the phonon scattering, and the magnetic scattering is clearly identified through momentum and temperature dependencies (see Fig. 3 of the main text). We note that the two lower phonon modes, which are common to many perovskite materials, are at energies which are not far from the zone-boundary magnon mode energies. Further single crystal inelastic neutron scattering measurements are required to determine whether this is a mere coincidence or a result of magnon-phonon coupling in this material.

[1]J. G. Bednorz and K. A. Muller, Z. Phys. B **189**, 64 (1986).

[2]S. Jin, T. H. Tiefel, M. McCormack, R. A. Fastnacht, R. Ramesh, and L. H. Chen, Science **264**, 413 (1994).

[3]Y. Maeno, H. Hashimoto, K. Yoshida, S. Nishizaki, T. Fujita, J. G. Bednorz, and F. Lichtenberg, Nature **372**, 532 (1994).

[4]R. A. Phillips and H. R. Shanks, Phys. Rev. B **4**, 4601 (1971).

[5]B. J. Kim, H. Jin, S. J. Moon, J.-Y. Kim, B.-G. Park, C. S. Leem, J. Yu, T. W. Noh, C. Kim, S.-J. Oh, J.-H. Park, V. Durairaj, G. Cao, and E. Rotenberg, Phys. Rev. Lett. **101**, 076402 (2008).

[6]Y. Singh and P. Gegenwart, Phys. Rev. B **82**, 064412 (2010).

[7]Y. Singh, S. Manni, J. Reuther, T. Berlijn, R. Thomale, W. Ku, S. Trebst, and P. Gegenwart, Phys. Rev. Lett. **108**, 127203 (2012).

[8]G. Jackeli and G. Khaliullin, Phys. Rev. Lett. **102**, 017205 (2009).

[9] A. Shitade, H. Katsura, J. Kuneš, X.-L. Qi, S.-C. Zhang, and N. Nagaosa, Phys. Rev. Lett. **102**, 256403 (2009).

[10] Y. Okamoto, M. Nohara, H. Aruga-Katori, and H. Takagi, Phys. Rev. Lett. **99**, 137207 (2007).

[11] M. J. Lawler, A. Paramekanti, Y. B. Kim, and L. Balents, Phys. Rev. Lett. **101**, 197202 (2008).

[12] D. Yanagishima and Y. Maeno, J. Phys. Soc. Jpn. **70**, 2880 (2001).

[13] W. Witczak-Krempa and Y. B. Kim, Phys. Rev. B **85**, 045124 (2012).

[14] X. Wan, A. M. Turner, A. Vishwanath, and S. Y. Savrasov, Phys. Rev. B **83**, 205101 (2011).

[15] G. Chen and L. Balents, Phys. Rev. B **84**, 094420 (2011).

[16] H. Gretarsson, J. P. Clancy, X. Liu, J. P. Hill, E. Bozin, Y. Singh, S. Manni, P. Gegenwart, J. Kim, A. H. Said, D. Casa, T. Gog, M. H. Upton, H.-S. Kim, J. Yu, V. M. Katukuri, L. Hozoi, J. van den Brink, and Y.-J. Kim, Phys. Rev. Lett. **110**, 076402 (2013).

[17] R. Arita, J. Kuneš, A. V. Kozhevnikov, A. G. Eguiluz, and M. Imada, Phys. Rev. Lett. **108**, 086403 (2012).

[18] I. I. Mazin, H. O. Jeschke, K. Foyevtsova, R. Valentí, and D. I. Khomskii, Phys. Rev. Lett. **109**, 197201 (2012).

[19] R. Comin, G. Levy, B. Ludbrook, Z.-H. Zhu, C. N. Veenstra, J. A. Rosen, Y. Singh, P. Gegenwart, D. Stricker, J. N. Hancock, D. van der Marel, I. S. Elfimov, and A. Damascelli, Phys. Rev. Lett. **109**, 266406 (2012).

[20] J. Longo and R. Ward, J. Am. Chem. Soc. **83**, 2816 (1961).

[21] A. W. Sleight, J. Longo, and R. Ward, Inorg. Chem. **1**, 245 (1962).

[22] K.-I. Kobayashi, T. Kimura, Y. Tomioka, H. Sawada, K. Terakura, and Y. Tokura, Phys. Rev. B **59**, 11159 (1999).

[23] D. Serrate, J. M. D. Teresa, and M. R. Ibarra, J. Phys.: Condens. Matter **19**, 023201 (2007).

[24] C. Azimonte, J. C. Cezar, E. Granado, Q. Huang, J. W. Lynn, J. C. P. Campoy, J. Gopalakrishnan, and K. Ramesha, Phys. Rev. Lett. **98**, 017204 (2007).

[25] B. C. Jeon, C. H. Kim, S. J. Moon, W. S. Choi, H. Jeong, Y. S. Lee, J. Yu, C. J. Won, J. H. Jung, N. Hur, and T. W. Noh, J. Phys.: Condens. Matter **22**, 345602 (2010).

[26] A. F. Garcia-Flores, A. F. L. Moreira, U. F. Kaneko, F. M. Ardito, H. Terashita, M. T. D. Orlando, J. Gopalakrishnan, K. Ramesha, and E. Granado, Phys. Rev. Lett. **108**, 177202 (2012).

[27] G. Jackeli, Phys. Rev. B **68**, 092401 (2003).

[28] A. B. Harris, T. Yildirim, A. Aharony, O. Entin-Wohlman, and I. Y. Korenblit, Phys. Rev. B **69**, 035107 (2004).

[29] L. Brey, M. J. Calderón, S. Das Sarma, and F. Guinea, Phys. Rev. B **74**, 094429 (2006).

[30] O. Erten, O. N. Meetei, A. Mukherjee, M. Randeria, N. Trivedi, and P. Woodward, Phys. Rev. Lett. **107**, 257201 (2011).

[31] Y. Krockenberger, K. Mogare, M. Reehuis, M. Tovar, M. Jansen, G. Vaitheeswaran, V. Kanchana, F. Bultmark, A. Delin, F. Wilhelm, A. Rogalev, A. Winkler, and L. Alff, Phys. Rev. B **75**, 020404 (2007).

[32] O. Nganba Meetei, O. Erten, M. Randeria, N. Trivedi, and P. Woodward, arXiv:1210.6687 (2012).

[33] K. I. Kobayashi, T. Kimura, H. Sawada, K. Terakura, and Y. Tokura, Nature **395**, 677 (1998).

[34] I. Žutić, J. Fabian, and S. Das Sarma, Rev. Mod. Phys. **76**, 323 (2004).

[35] W. Prellier, V. Smolyaninova, A. Biswas, C. Galley, R. L. Greene, K. Ramesha, and J. Gopalakrishnan, J. Phys.: Condens. Matter **12**, 965 (2000).

[36] A. Winkler, N. Narayanan, D. Mikhailova, K. G. Bramnik, H. Ehrenberg, H. Fuess, G. Vaitheeswaran, V. Kanchana, F. Wilhelm, A. Rogalev, A. Kolchinskaya, and L. Alff, New J. Phys. **11**, 073047 (2009).

[37] G. E. Granroth, D. H. Vandergriff, and S. E. Nagler, Physica B Condensed Matter **385-86**, 1104 (2006).

[38] G. E. Granroth, A. I. Kolesnikov, T. E. Sherline, J. P. Clancy, K. A. Ross, J. P. C. Ruff, B. D. Gaulin, and S. E. Nagler, J. Phys.: Conf. Ser. **251**, 012058 (2010).

[39] The different atomic form factors of Re and Fe have not been taken into account in the theoretical calculations; however, their form factors only differ by about 15% from the average form factor at the largest Q. Since the dispersing modes do not strictly have Re or Fe character, we expect taking form factors into account will slightly modify the intensities in our theoretical plots.

[40] When projected to t_{2g} subspace, the effective orbital angular momentum becomes $L_{\mathrm{eff}} = 1$ with opposite sign. We drop the subscript and use this L in the following discussions.

[41] Note that we use $\mathcal{R}$ for the effective total angular momentum for a Re ion. $\mathcal{R} = 2$ would correspond to $j_{\mathrm{eff}} = 2$ if we borrow the notation commonly used in iridate literature.

[42] T. A. Kaplan, Phys. Rev. **109**, 782 (1958).

[43] H. Wu, Phys. Rev. B **64**, 125126 (2001).

[44] P. Fazekas, *Lectures Notes on Electron Correlation and Magnetism* (World Scientific, Singapore, 1999).

[45] G. L. Squires, *Introduction to the Theory of Thermal Neutron Scattering* (Dover, London, 1978).